Solid Earth

Discussions

Open Access

EGU

Matrix gas flow through 'impermeable' rocks - shales and tight sandstone

Ernest Rutter[1], Julian Mecklenburgh[1], Yusuf Bashir[1,a]

[1]Rock Deformation Laboratory, Dept. of Earth and Environmental Sciences, University of Manchester, Manchester M13 9PL, UK.

[a]Now at: Department of Petroleum Resources, Abuja, Nigeria.

Correspondence to : E. Rutter (e.rutter@manchester.ac.uk)

Abstract. The effective pressure sensitivity of gas flow through two shales (Bowland and Haynesville shales) and a tight gas sandstone (Pennant sandstone) was measured over the typical range of reservoir pressure conditions. These are low permeability rocks such as can be exploited as caprocks above reservoirs that might be developed to store compressed air, methane, hydrogen or to bury waste carbon dioxide, all of which may become important components of the forthcoming major changes in methods of energy generation and storage. Knowledge of the petrophysical properties of such tight rocks will be of great importance in such developments. All three rocks display only a small range in $\log_{10}$ permeability at low pressures, but these decrease at dramatically different rates with increasing effective pressure, and the rate of decrease itself decreases with pressure, as the rocks stiffen. The pressure sensitivity of the bulk moduli of each of these rocks was also measured, and used to formulate a description of the permeability decrease in terms of the progressive closure of narrow, crack-like pores with increasing pressure. In the case of the shales in particular, only a very small proportion of the total porosity takes part in the flow of gases, particularly along the bedding layering.

Key words: Permeability. shales, sandstone, bulk modulus, pressure sensitivity, gas porous flow

Supplementary data file: DF1.csv at   https://zenodo.org/record/5675601

1. Introduction

Shales (laminated mudstones) are of particular importance because their fine grain size and tight pore structure gives them a particularly low matrix permeability and hence makes them excellent cap rocks for the containment of oil, water and gases. This includes their future use as a sealant for the storage containment of fuel gases hydrogen and methane, compressed air storage and for the disposal deep underground of waste liquids and gases, including waste carbon dioxide. Organic shales are source rocks for petroleum and become source, reservoir and seal for unconventional natural gas (shale gas). The enormous economic importance of shales cannot be overstated, and this demands an ever-increasing understanding of their petrophysical properties.

Compared to conventional reservoir rock materials (sandstones, limestones), shales are particularly difficult to work with. Their commonly laminated nature makes them often highly fissile, with a tendency to split along the layering. Thus coring and cutting operations for sample preparation are often difficult, and their physical properties (elasticity, mechanical strength, permeability, elastic wave velocities) are generally anisotropic. Determination of properties that involve working with elevated pore pressures become time-dependent, according to the slow rates of fluid permeation though the microstructure in response to applied effective pressure changes, and the rock itself may display time-dependent deformation (creep) under load. Mineralogically, shales can be highly variable, particularly with respect to the relative proportions of the major mineral components: framework silicates, clays and other phyllosilicates, and carbonates (Lazar et al. 2015; Diaz et al. 2013; Dowey andTaylor 2020), and this can be expected to be reflected in the spectrum of petrophysical properties of shales.

Solid Earth
Open Access
Discussions

EGU

40 In contrast to shales, tight gas sandstones (e.g. Zee Ma et al., 2016)) may display similarly low permeabilities

41 and porosities, but lack extreme fissility and typically possess a matrix of coarser-grained framework silicate

42 minerals (quartz and feldspar) but with primary pore spaces filled with some detrital micas but also authigenic

43 growths of clay minerals and hydrated oxide phases. Thus their properties tend to form an upper (more permeable

44 and less anisotropic) bound to the range of properties displayed by shales. For this reason, we have included for

45 comparison in this study such a rock type. Here also we present a study of the matrix permeability of two, rather

46 different shales. Permeability and storativity were measured parallel to the layering under hydrostatic loading

47 conditions as a function of total confining pressure and pore pressure of argon gas, and normal to layering at one

48 pore pressure only. Results were fitted to a simple physical model. The spectrum of behaviours observed provides

49 insight into the physical controls on the matrix permeabilities of these rocks.

50 **2. Sample materials and characterization**

51 Two shale samples recovered from depth in boreholes were used. The samples are strikingly mineralogically

52 and microstructurally different. They were characterized mineralogically by quantified X-ray diffraction analysis,

53 which was also used to estimate grain density using published mineral densities. All samples were oven dried at

54 60 ºC until constant weight (at least one week), and then maintained at that temperature until use. All experiments

55 were carried out in this oven dried state. Other than with the degree of water saturation in the as-supplied state, it

56 can be very difficult to test shales with varying degrees of controlled or with total water saturation. The sandstone

57 studied was from a surface exposure but was treated in the same way as the shales.

58 **2.1 Pennant sandstone.**

59 This is a hard, grey marine sandstone (Fig. 1a and b) of upper Carboniferous age (Kelling 2017), that outcrops
60 in south Wales, Great Britain. We have previously reported rock mechanics studies on this rock in Hackston and
61 Rutter (2016) and Rutter and Hackston (2017). All measurements reported were made normal to bedding. Bedding
62 planes are not apparent in hand specimen.

63 Modal proportions (vol% solids):   Quartz + Feldspar 73.73 ; Phyllosilicates 9.81 ; (estimated uncertainties $\pm$
64 4% of cited percentages)

65 Grain density 2661 $\pm$ 120 kg/m^3 : Bulk density 2558 $\pm$ 35 kg/m^3: Total porosity 3.89 $\pm$ 0.04 % from XRD,
66 4.60% $\pm$ 0.01 using a helium porosimeter.

67 **2.2 Bowland Shale.** This is a phyllosilicate-rich, carbonate-poor siliceous mudstone (Fig. 1c), very pyrite-rich,
68 (8.3 wt%), of Lower Carboniferous age. It was the target formation for exploitation of shale gas in Northern
69 England.

70 Depth 2060.55 m. Provider sample identifier IG 5-8W. Location: west Manchester, UK.

71 Modal proportions (vol% solids):   Quartz + Pyrite 38.4 ; Phyllosilicates 61.6 ; Carbonates 0 (estimated
72 uncertainties $\pm$ 4% of cited percentages)

73 Grain density 2842 $\pm$ 120 kg/m^3 : Bulk density 2714 $\pm$ 38 kg/m^3: Total porosity 4.50 $\pm$ 0.02% from XRD; 4.6% $\pm$ 0.1
74 using a helium porosimeter.

75 Total organic carbon 1.14 $\pm$ 0.2 wt% ; Water loss from drying 0.74 $\pm$ 0.15 vol% , hence initial water saturation =
76 13%.

77 **2.3 Haynesville Shale**

Solid Earth

Discussions

Open Access

EGU

3

78   This is a phyllosilicate-poor, carbonate-rich siliceous mudstone (Fig. 1d). Pyrite-poor (0.7 wt%), of Upper

79   Jurassic age (Hammes et al. 2011), successfully exploited for shale gas in the southern United States.

80   Depth 3730.6 m. (Sample identifier). Location: Hewitt Land LLC well, Caspian Field, de Soto parish, Louisiana,

81   USA.

82   Modal proportions (vol% solids):   Quartz + Feldspar + Pyrite 34.5;   Phyllosilicates 13.4;   Carbonates 52.1;

83   (estimated uncertainties ± 4% of cited percentages)

84   Grain density 2703 ± 120 kg/m^3:   Bulk density 2453 ± 35 kg/m^3: Total porosity 9.26 ± 0.04 % from XRD, $7.6\% \pm 0.1$

85   using a helium porosimeter. Total organic carbon 1.3 ± 0.2 wt%.
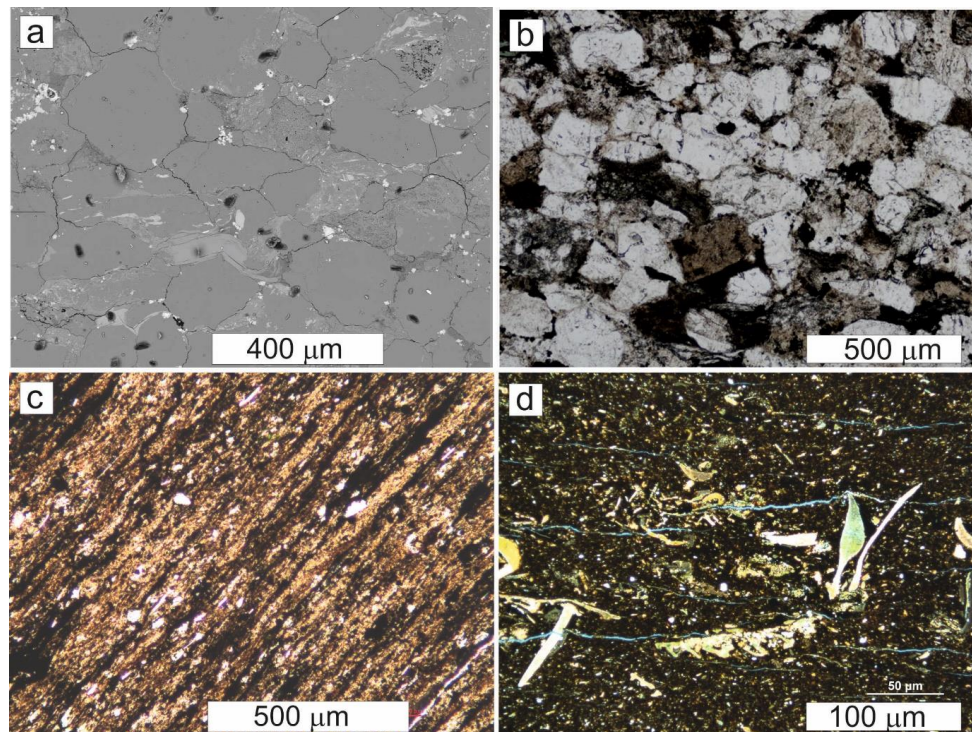
87   **Figure 1. Microstructures of the rocks tested.**

88   **(a) Back-scattered electron (BSE) image and (b) optical image (PPL) of Pennant sandstone, bedding**

89   **horizontal, showing large quartz grains (mid-grey in (a)) with sutured contacts caused by pressure solution**

90   **and remaining pore spaces largely filled by iron hydroxide (white in (a)) and authigenic clay minerals (light**

91   **grey in (a)), reducing the overall porosity to 4.6%**

92   **(c) Microstructure (Plane-polarized light (PPL) image of polished thin section) of Bowland shale, finely and**

93   **homogeneously banded with elongate clusters of organic material and pyrite (black) and silt-sized grains of**

94   **quartz in a matrix of elongate clusters of phyllosilicate (clay + detrital micas) grains.**

95   **(d) Microstructure of Haynesville shale. (PPL image of polished thin section, horizontal dimension is**

96   **parallel to layering). Bioturbation destroys continuity of layering. Rock is only weakly banded but**

97   **nevertheless fissile; bedding-parallel cracks can be seen, opened during thin-section preparation.**

98   **Calcareous fossil fragments and authigenic calcite-filled voids, in matrix of finer grained phyllosilicate**

99   **(clays + detrital micas) and fine silt-sized framework silicates.**

Solid Earth

Discussions

Open Access

EGU

100   Defining velocity anisotropy as $2(V_{max} – V_{min})/(V_{max} + V_{min})$, the anisotropies of Bowland and Haynesville shales
101   are respectively 30.7% and 32.2% at 100 MPa total confining pressure. The velocity anisotropy of Pennant
102   sandstone at elevated pressure was not determined. It is 15.5% axial and 3.1% radial at room pressure, but will be
103   less at elevated pressure.

104   The wt% values for the mineralogical composition of all rock types were converted to vol% using tabulated
105   densities from the literature (Mavko et al., 2009; Mondol et al., 2008), and together with averaged mineral elastic
106   properties the bulk elastic properties of the rocks estimated were as Voigt-Reuss-Hill (VRH) averages assuming
107   zero porosity. These are listed in Table 1.

108   Some comparisons of behaviour are made with previously published (Mckernan et al., 2017) data on Whitby
109   shale. This is a well-foliated, silt-bearing, clay-rich, carbonate-poor mudstone of Liassic age, with 8.1% total
110   porosity and 1.5% volume amorphous organic matter.

111

112

113   **Table 1. Phase fractions, mineral densities and Voigt-averaged bulk and shear moduli K_v and G_v (from**
114   **literature) and calculated zero porosity elastic moduli as Voigt-Reuss-Hill (VRH) averages (GPa) for**
115   **Bowland and Haynesville shales and for Pennant sandstone. Organic fraction not included. Mineral phase**
116   **Reuss-average elastic moduli can be calculated from the other values supplied. K_0 = bulk modulus, G_0 =**
117   **shear modulus, E_0 = Young's modulus (VRH-averaged whole-rock values assuming isotropy). Modal**
118   **volume percent is % of the solids.**

119

Bowland Shale IG5-8WC

Phase	Wt%	±Error%	Density kg m^{-3}	Vol%	Kv GPa	Gv GPa
Quartz	30.98	1.42	2648	33.64	12.73	14.90
Pyrite	8.32	0.44	5020	4.77	6.63	5.36
Muscovite 2M	60.44	2.04	2844	61.11	35.55	21.61
Kaolinite	0.26	2.60	1580	0.48	.0072	.0067
Total	100.0			100.0		
Zero porosity moduli (GPa):	VRH(K_o)		VRH(G_o)		VRH(E_o)	
	52.79		40.69		97.13	

120

Haynesville Shale YB03

Phase	Wt%	±Error%	Density kg m^{-3}	Vol%	Kv GPa	Gv GPa
Albite	10.49	0.505	2610	11.01	5.59	3.22
Ankerite Fe0.55	4.65	0.36	3050	4.17	4.80	2.46
Calcite	47.22	1.25	2712	47.69	32.94	15.24
Clinochlore IIb-24.11	0.41	2.90	3880	2.26	1.37	
Muscovite 1M	9.97	1.46	2844	9.50	5.27	3.36
Pyrite	1.27	0.10	5020	0.69	.958	.775
Quartz	18.71	0.74	2648	19.35	7.32	8.57
Siderite	0.47	0.07	3960	0.33	.408	.168
Orthoclase	3.20	0.46	2540	3.45	1.61	.815
Total	100			100.1		
Zero porosity moduli (GPa)				VRH(G_o)	VRH(E_o)	VRH(K_o)
				60.57	34.91	87.86

121

Pennant Sandstone Pe2						
Phase	Wt%	±Error%	Density kg m^{-3}	Vol%	Kv GPa	Gv GPa
Albite	16.14	0.70	2610	16.46	8.20	4.72
Phyllosilicates	10.48	1.5	2840	9.81	6.10	3.71
Quartz	73.37	2.8	26480	73.73	27.77	32.50
Total	99.99			100.0		
Zero porosity moduli (GPa):				VRH(K$_o$)	VRH(G$_o$)	VRH(E$_o$)
				41.55	40.42	91.57

122

123   ---

124   **3. Experimental Methods**
125   **3.1 Permeability measurements**

126   Permeability measurements were made on cylindrical samples of either 25.4 or 20 mm nominal diameter, cut to

127   lengths of the same order or shorter. The latter is generally necessary for very low permeability rocks, but quite

128   apart from this it was not possible to obtain long cores from slabbed drill cores of the shales. Problems were also

129   encountered during shale specimen preparation owing to the friable nature of these materials. Porous sintered

130   stainless steel (316L) filter plates (17% porosity) were placed at either end of the sample to spread the pore fluid

131   uniformly over the ends of the rock samples. The assembly was jacketed in a heat-shrinkable polymer jacket, so

132   that pore fluid pressures less than the confining pressure could be applied. Confining pressures (hydraulic oil, a

133   synthetic ester, di-octyl sebacate, trade name Reolube DOS®) ranging up to a little over 100 MPa were used. This

134   fluid has the advantage of a relatively small rate of change of viscosity with pressure (see Rutter and

135   Mecklenburgh 2017 and 2018 for further details). In all experiments argon gas was used as the pore fluid, at

136   pressures ranging up to 80 MPa. The higher viscosity of a liquid pore fluid would have led to very long

137   experimental durations. The confining and pore pressures ranges cover the full extent of likely pressures to be

138   encountered in engineering operations to depths of *ca* 4 km.

139   Although it was intended that experiments would be carried out under hydrostatic confinement conditions, the

140   presence of a contrast in elastic properties of the specimen against the porous end plates and the steel loading

141   pistons induces a shear stress along these interfaces. This in turn causes the stress state in the specimen to deviate

142   from hydrostatic and to reduce the average mean stress. Deviations from hydrostatic loading are most severe when

143   the length of the specimen becomes less than twice the diameter. For this reason, mechanical testing of rocks is

144   usually carried out on specimens with a length:diameter ratio of 2.5:1 or more. Finite element analysis (FEA) of

145   the stress state in rocks confined between steel end plates were carried out to assess the expected departures from

146   hydrostatic loading, and the effects predicted must be borne in mind when interpreting the permeability data.

147   **Table 2. Elastic constants of the components in the finite element models.**

	Young's Modulus E GPa	Poisson's Ratio
Sample	60	0.250
Piston	190	0.265
Spacer (17% Porosity)	108.6	0.260

148

149
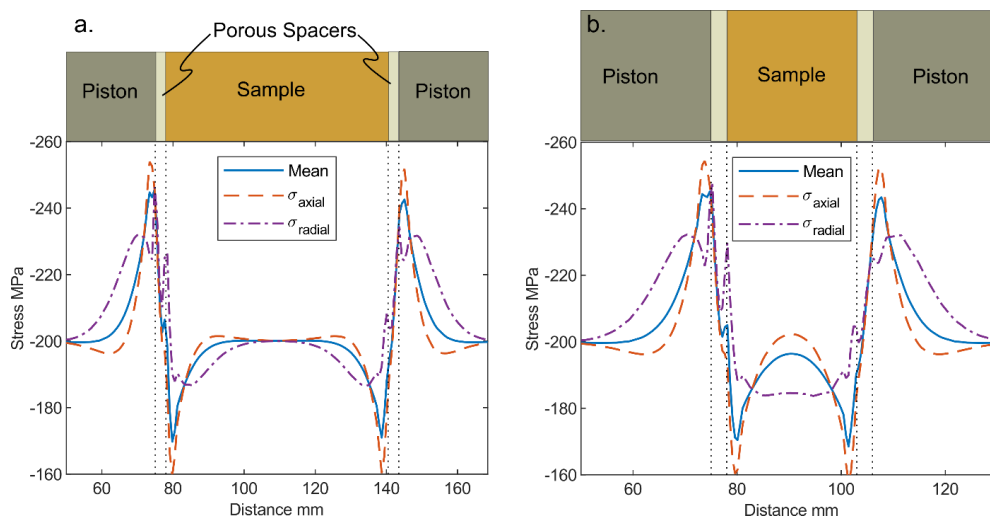
Figure 2. Results of finite element analyses showing stress profiles of mean stress, axial normal stress and radial normal stress along the axes of samples respectively of length:diameter ratios (a) 2.5:1 and (b) 1:1, each with a diameter of 25.4 mm. At the top of each figure is a scaled schematic of the assembly; notice the aspect ratio of the sample in each case. Externally applied hydrostatic stress was 200 MPa. For the longer sample the stress state in the greater part of the sample was near homogeneous, but for the shorter one a differential stress on the order of 7% of the applied hydrostatic stress was induced.

Figure 2 presents the results of finite element analyses showing stress profiles along the axes of samples respectively of length:diameter ratios (a) 2.5:1 and (b) 1:1, with a hydrostatic pressure of 200 MPa applied to the outer cylindrical surfaces. At each end of the sample a 3 mm thick, porous sintered steel disk was placed. Positions of boundaries between the solid steel pistons, the porous disks and the sample material are indicated. In both cases the sample diameter was 25.0 mm. Along-axis stress component variations were more varied than across the radius. Most of the stress heterogeneity (departure from the applied 200 MPa hydrostatic pressure) resides in and immediately adjacent to these disks, and for each stress component is of similar magnitude for both specimen lengths. Within the greater part of the sample volume in each case the axial normal stress is higher than the radial normal stress, and these components are similar to the principal stress values. For the longer sample, the stress state is near hydrostatic over 0.8 of the specimen length, but in the case of the shorter sample the stress components are notably non-hydrostatic over most of the specimen length, with maximum differential stress reaching 15 MPa (7% of the applied hydrostatic stress) in the central part of the sample.

A small number of permeability measurements were made using the pulse-transient-decay method of Brace et al. (1968), as modified by Cui et al. (2009). However, most experimental results were obtained using the oscillating pore pressure method (Kranz et al., 1990; Fischer and Paterson, 1992; Faulkner and Rutter, 2000; Bernabé et al., 2006; Mckernan et al., 2017). Whilst keeping the confining pressure constant and after establishing a constant pore pressure in the sample, a sinusoidal oscillation of pore pressure, of known period and of amplitude about 1 MPa, is applied at one end of the sample (upstream). As the pressure wave propagates through the sample it is phase-shifted and loses amplitude. The amplitude ratio (gain) and phase shift angle are measured. The solution to

176 the transport equation for these measured parameters is given by Bernabé et al., (2006) in terms of two

177 dimensionless numbers, η and ξ, from which permeability and sample storativity can be calculated using

187
$$\xi = \frac{SL\beta}{\beta_D}, \quad \eta = \frac{STk}{\pi L\mu\beta_D} \qquad (1)$$

178 Here, S is cross sectional area of the sample (normal to flow path), L is specimen length, β_D is downstream

179 volume storativity and β is specimen storativity, T is the period of the pore pressure oscillation, k is specimen

180 permeability, and μ is viscosity of the pore fluid. Argon gas viscosity as a function of pressure data was reported

181 by Michels et al., (1954). Storativity is the product of the volume of the void space concerned, with the pore fluid

182 (isothermal) gas compressibility. Argon compressibility is non-linear over the pore pressure range used (Gosman

183 et al., 1969) and substantially non-ideal above about 20 MPa. $\xi \approx \phi V_s / V_d$ where ϕ is specimen effective porosity,

184 V_s is total specimen volume and V_d is downstream reservoir volume. It cannot be assumed that effective

185 (conductive) porosity estimated from permeability measurements will necessarily be equal to total porosity

186 measured independently.

188 The apparatus used was the same as used for experiments reported by Rutter and Mecklenburgh (2017; 2018).

189 Pressure transducers with a resolution of 0.02 MPa were used for pore pressure measurements, and confining

190 pressure was measured to an accuracy better than 0.3 MPa. The minimum pore pressure used was 10.0 MPa. This

191 is sufficiently high to avoid exsorption of gas from mineral surfaces and to avoid slip flow of gas through pore

192 spaces (Knudsen/Klinkenberg effect, Mckernan et al. 2017). It was determined that the experimental assembly

193 shows no detectable gas flow when a rock sample is replaced by an impermeable steel plug.

194 **3.2 Error, uncertainty and reproducibility**

195 Accuracy of reported permeability depends on uncertainties of the parameters in Eq. (1). η and ξ can be

196 measured to within about 2% of the true value, and S, T L and μ to within 1%. The least certainly known

197 parameter is the downstream volume, which is determined as the difference between the total volume of the pore

198 pressure pipework measured with and without the downstream pipework connected, each measured by the pore

199 pressure change produced by a known volumometer piston displacement. The downstream reservoir volume V_d

200 was measured to be 445 ± 30 mm³, including the volume of the downstream porous steel filter. These

201 uncertainties translate to an accuracy of $\log_{10}$ permeability of ± 0.1 log units. This is small, given that permeability

202 varies with pressure by 1 to 3 orders of magnitude.

203 The largest apparent uncertainties in reported permeability data arise from hysteretic changes in the behaviour of

204 the rock itself as effective pressure is cycled and will be discussed when the data are presented.

205 **3.3 Bulk modulus measurements**

206 Bulk modulus measurements as a function of confining and pore pressures were made as far as possible on

207 physically the same samples that were used for the permeability measurements, to avoid any influence of

208 mineralogical or microstructural differences. Measurements were made over a range of total confining pressures

209 up to 200 MPa, after the permeability measurements were made, with constant pore pressures of argon gas,

210 typically at nominally 10, 35, 67 and 100 MPa. The method involved measuring volume of pore fluid (argon gas)

211 progressively expelled as the total confining pressure was increased at constant pore pressure. This measures the

212   compressibility of the pore spaces. P-wave acoustic velocity measurements were made at the same time, although
213   these data are not reported here.

214   Unlike for permeability measurements, porous steel plates were not used at the ends of the specimens for pore
215   fluid displacement measurements. For the relatively porous and permeable Haynesville shale and Pennant
216   sandstone, a short hole, normally 15 mm long and 1.5 mm diameter, was drilled into the end of the specimen
217   facing the pore pressure inlet pipe, to facilitate flow of gas into and out of the specimen. This was thought to be
218   unlikely to be adequate for the lower porosity and permeability Bowland shale, therefore samples were cut in half
219   parallel to the long axis so that a 2mm thick, porous steel plate could be inserted, to facilitate gas flow over a wide
220   surface area of the rock, yet without affecting the P-wave velocity along the length of the specimen.

221   When considering the results, the procedure for pressure application is of importance. For the tests with pore
222   pressure, the application of a confining pressure slightly greater than the eventual pore pressure was made,
223   followed by application of the pore pressure. Then the total confining pressure was increased stepwise away from
224   the constant pore pressure. Thus tests at high pore pressure have been exposed to much higher effective pressures
225   before application of pore pressure, than when the test pore pressure is to be low.

226   When pore pressure was made non-zero, constant pore pressure was maintained using a servo-controlled pore
227   volumometer. Each applied increment of the confining pressure caused a small elastic contraction of the pore
228   volume that attempts to raise the pore pressure. The servo-controller backs off the moveable piston in the pore
229   volumometer in order to keep the pore pressure constant. The distance swept by the volumometer piston at
230   constant pore pressure allows the volume of gas expelled to be measured to a resolution of 0.4 mm^3. In this way
231   the history of *pore volume* change at constant pore pressure during progressive loading by the confining pressure
232   can be determined. The compressibility of the pore space C_{pc} is given by the fractional change in pore volume V_p
233   in response to a change in confining pressure P_c at constant pore pressure P_p (Zimmerman, 1991), and is the
234   reciprocal of the dry pore space bulk modulus K_ϕ :

238
$$C_{pc} = \frac{1}{K_\phi} = \frac{1}{V_p}\left(\frac{\partial V_p}{\partial P_c}\right)_{Pp} \qquad (2)$$

235   Note $V_p = \phi V_b$, where V_b is the total sample volume. K_{dry} is the bulk modulus of the porous aggregate. Its
236   reciprocal, compressibility C_{bc} , the bulk volume change in response to a change in confining pressure at constant
237   pore pressure, is defined by

239
$$C_{bc} = \frac{1}{K_{dry}} = \frac{1}{V_b}\left(\frac{\partial V_b}{\partial P_c}\right)_{Pp} \qquad (3)$$

240   where V_b is the bulk volume, including the pore space. The zero-porosity bulk modulus of the constituent mineral
241   aggregate is defined as K_o (Table 1), then the dry bulk modulus K_{dry} ($= K_{bc}$) is given (Mavko et al., 2009) by

242
$$\frac{1}{K_{dry}} = \frac{1}{K_o} + \frac{\phi}{K_\phi} \qquad (4)$$

243   Decrease in permeability with increasing Terzaghi effective pressure ($P_c - P_p$) (Terzaghi, 1923) is primarily due to
244   the pressure dependence of K_{dry}, leading to progressive closure of pore space. Thus the independent determination of
245   K_{dry} from pore volumometry measurements provides a basis for the interpretation of the pressure sensitivity of
246   permeability.

247   Note that we have no means of measuring directly the influence of pore pressure change on bulk deformation of

248   the sample, characterized by the compressibility C_{bp}, or

249
$$C_{bp} = \frac{1}{K_{bp}} = \frac{1}{V_b}\left(\frac{\partial V_b}{\partial P_p}\right)_{P_c} \qquad (5)$$

250   This would require strain gauges or equivalent to be mounted on the outer surface of the rock sample (e.g.

251   Hasanov et al., 2019, 2020). However, it can be obtained from

253
$$\frac{1}{K_{bp}} = \frac{1}{K_{bc}} - \frac{1}{K_o} \qquad (6)$$

252   (Mavko et al., 2009).

254   Biot and Willis (1957), Skempton (1960) and Nur and Byerlee (1971) obtained a theoretical expression for the

255   effective pressure coefficient (Biot coefficient) m for elastic *deformations* (including deformations of pore spaces)

256   of a mechanically linear, homogeneous and isotropic rock, so that effective pressure $P_{eff} = (Pc - mP_p)$, and

257
$$m = 1 - \frac{K_{dry}}{K_o} \qquad (7)$$

258   Note that this effective pressure coefficient is not necessarily the same as that describing empirically the influence

259   of pore pressure on permeability, nor on elastic wave velocities nor the failure characteristics of rocks (whether

260   frictional sliding or intact rock failure).

261   m is also given by

262
$$m = \frac{K_o}{K_{bp} + K_o} = \frac{K_o - K_{bc}}{K_o} = 1 - \frac{K_\phi}{K_\phi + K_0\phi} \qquad (8)$$

263   Sample storativity is related to these stiffness parameters by

264
$$\beta = \frac{1}{K_{bp}} + \phi\left(\frac{1}{K_f} - \frac{1}{K_o}\right) \qquad (9)$$

265   where K_f is pore fluid bulk modulus (Hasanov et al., 2019).

266   In all calculations we assume K_o is negligibly sensitive to effective pressure, compared to porous rock stiffnesses

267   such as K_{dry}, following data for K_o for minerals such as quartz via ultrasonic measurements (e.g. Calderón et al.,

268   2007, who give $K_o = 37.5(GPa) + 4.7*P(GPa)$).

269   **4.   Experimental results**

270   A full tabulation of experimental results is given in the supplementary data file DF1.

271   **4.1 Permeability results**

272   Experimental conditions and results are presented graphically in Figs. 3 through 8. The first pressure cycle

273   applied to most rocks results in higher permeabilities and a relatively rapid rate of decrease of permeability with

274   pressure, as inelastic cracks become progressively and permanently closed. Subsequent pressure cycles up to the

275   maximum pressure previously attained are more nearly elastic and reproducible, although there can be a small

276   tendency to reduce permeability slightly with subsequent pressure cycles. The first stage in a suite of permeability

277   measurements covering a wide range of confining and pore pressures therefore must be to take the sample to the

278   maximum effective pressure to which it is to be exposed, to ensure closure of these inelastic cracks and pores up

279   to that pressure.

4.1.1 Form of data and reproducibility

281   In the regime of elastic behaviour permeability (as log k) is not usually linear neither on a k vs P_c plot nor even

282   on a log k vs P_c plot but is concave upwards (Fig. 3). The decrease of permeability with effective pressure is due

283   to elastic closure of conductive cracks and pores, and this is expected to become more difficult as the porous

284   material stiffens at higher pressure. Thus although it is common, and useful for the purpose of modelling reservoir

285   behaviour (e.g. Kwon et al., 2001; Bustin et al., 2008; Cui et al., 2009; Heller et al., 2014; Mckernan et al., 2017)

286   to describe quantitatively the relationship between $\log_{10} k$ and P_c by making a least-squares linear fit to the data, a

287   better description would take into account the curvature.

288   In order to estimate the reproducibility of the permeability data, a determination of the standard error was made

289   about a polynomial fit to the 10 MPa pore pressure data (after the first pressure cycle) for each rock type. For

290   Bowland shale it is ±0.22 $\log_{10} k$ units, for Haynesville shale it is ±0.19 $\log_{10} k$ units and for Pennant sandstone it is

291   ±0.10 $\log_{10} k$ units.

4.1.2 Influence of confining (Pc) and pore pressures (Pp) on permeability
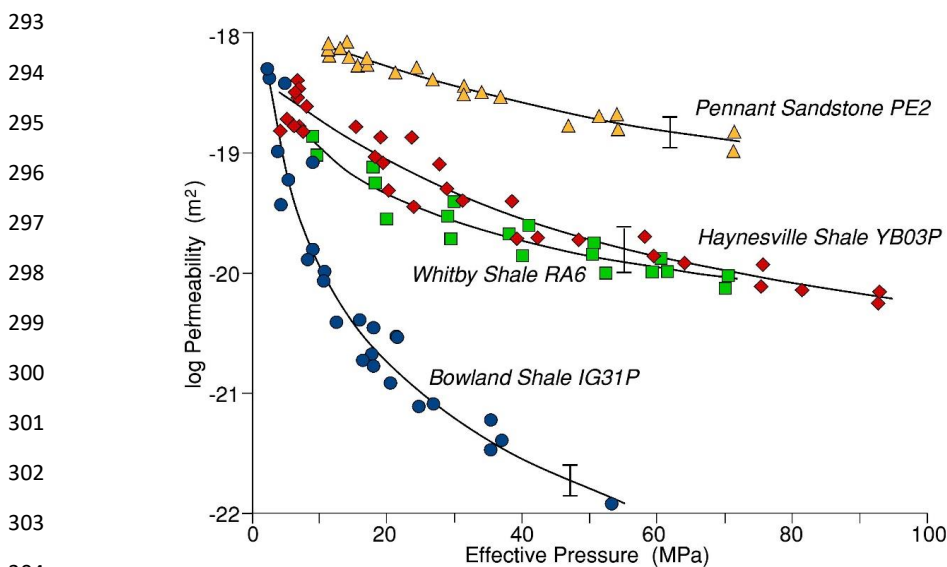

Figure 3. Matrix permeability of Pennant sandstone for flow normal to bedding, and for Bowland and Haynesville shales for flow parallel to layering, as a function of Terzaghi effective pressure (P_c – nP_p) over a wide range of pore pressures of argon gas. Data of Mckernan et al. (2017) for Whitby shale sample RA6 at a constant argon gas pore pressure of 25 MPa are also shown for comparison. In each case data from the first pressure cycle up to the maximum effective pressure attained has been excluded. All rocks show permeability decreasing more slowly with effective pressure at higher effective pressures. Error bars are shown as estimated for the 10 MPa pore pressure data.

312   Figure 3 shows the influence of Terzaghi effective pressure on matrix permeability over a range of pore

313   pressures, for Haynesville and Bowland shales for flow parallel to layering and for Pennant sandstone normal to

314   bedding after the first pressure cycle. They are expressed as $\log_{10} k$ versus effective pressure (P_c – nP_p), where

315 the pore pressure parameter $n = 0.86$ for Pennant sandstone and is 0.99 for Haynesville shale. For the Bowland

316 shale the data showed that permeability varied over almost four orders of magnitude, much greater than for the

317 other two rock types, and as a result it was evident that parameter n tended to increase with the value of Terzaghi

318 effective pressure, varying from unity at low pressures to 1.6 at high effective pressures. The least squares best-

319 fit curve to each of these data sets is shown in Fig. 3. For all three rocks the form of the behaviour is similar, each

320 showing a decreasing slope at higher effective pressures, as would be expected from pressure-induced

321 constriction of pore spaces. The Pennant sandstone showed the least sensitivity to effective pressure variations,

322 whilst the Bowland shale displays a far greater sensitivity to effective pressure. The Haynesville shale takes an

323 intermediate position that is closely comparable to the data for Whitby shale (sample RA6 taken from the data

324 reported by Mckernan et al. 2017 for pressure cycles 2, 3. 4 and 5).

325   Whilst these rocks display relatively small differences in permeability at low effective pressures, increase in

326 pressure results in markedly divergent trends, resulting in large differences in permeability developing over the

327 range of effective pressures expected to encountered under reservoir conditions. This observation emphasises the

328 importance of understanding the pressure sensitivity of shales that are to be exploited for engineering purposes.

329 **4.1.3 Influence of flow direction at constant pore pressure.**

330
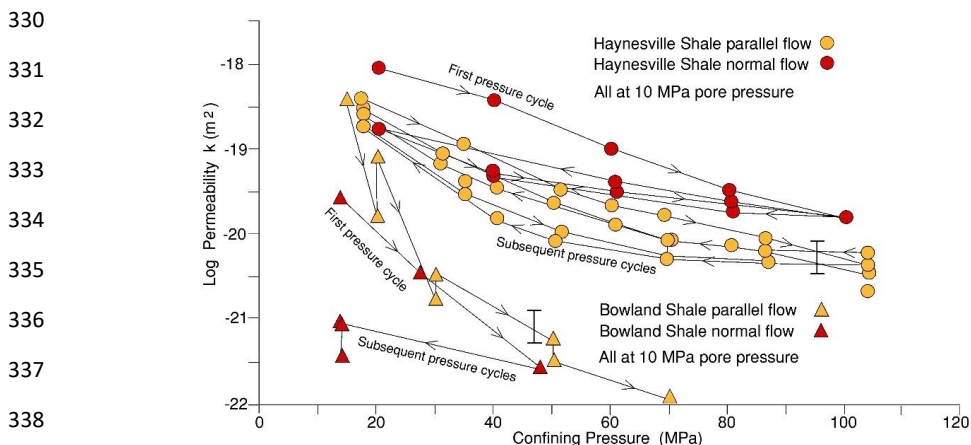
Figure 4. Comparison of data at 10 MPa pore pressure for flow parallel and normal to layering in the two shales. Parallel flow data are shown without the first pressure cycle, during which some pores become permanently closed. Normal-to-layering flow data are shown including the first pressure cycle. For Bowland shale, flow normal to layering is slower, but for Haynesville shale there is little effect, except that pressure sensitivity is less for flow normal to layering.

344   Flow normal to layering in shales is often much slower than flow parallel to layering, but not always. Layer-

345 normal flow was therefore measured for these rocks using shorter samples than for flow along the layering, and

346 only at 10 MPa argon pore pressure (Fig. 4). However, for Haynesville shale the direction of flow makes little

347 difference, except that pressure sensitivity is reduced for layer-normal flow, as would be expected if flow parallel

348 to the layering is dominated by low aspect ratio, crack-like pores that are relatively compressible. The different

349 pressure sensitivities of permeability mean that (after the first pressure cycle) flow along the layering becomes

350 faster at low effective pressures, but slower at higher effective pressures. Bowland shale shows a small reduction

351 in permeability for flow normal to layering relative to parallel to layering (post the first pressure cycle), and there

352 is also some indication of a reduced pressure sensitivity, although the dataset is small.

4.1.4 Storativity of the rocks

353

354   Oscillating pore pressure permeametry yields a dimensionless permeability parameter η and a dimensionless

355   storativity parameter ξ (Eq. (1)), which is the ratio of the accessible pore volume in the rock to the downstream

356   reservoir volume. A plot of experimentally measured log gain vs signal phase shift angle lies along a line of constant ξ

357   if the sample storativity is constant (Fig. 5). Thus the effective (conductive) porosity of the sample during the course

358   of the experiment can be calculated. The conductive porosity of many rocks is smaller than the total porosity.

359   The total porosity also corresponds to a particular value of ξ. If all of the porosity were to be involved in the flow,

360   these ξ values will be equal. Note that a value of $\xi = 1$ corresponds to the downstream volume of the apparatus being

361   equal to the pore volume of the rock sample. A storativity can also be calculated from data from elastic pore

362   compressibility measurements. Hasanov et al. (2019) calculated storativity in these two ways.

363   Figure 5a shows log gain vs phase angle data for Haynesville shale for flows both parallel and normal to layering.

364   Figure 5b shows corresponding data for Bowland shale and Pennant sandstone, but insufficient data was obtained for

365   Bowland shale normal to layering, given its much lower permeability. For flow along the layering, both of the shale

366   types show $\xi < 0.1$, corresponding to the conductive porosity being much smaller ($< 1\%$) than the total porosity of the

367   rocks (respectively 4.5% and 9.3%). Thus whilst the bulk of the pore space can contribute to gas storage, only a very

368   small fraction of well-connected porosity contributes to gas flow along the layering in the shales.

369   The log gain vs phase angle data was non-linear least-squares fitted to obtain an average value for ξ for each rock

370   type, subject to the constraint that ξ is constant. For Haynesville shale for flow across the layering ξ lies along the

371   trend $\xi = 0.39$, corresponding to a conductive porosity of ~6.0%. Thus flow across the layering 'sees' more of the

372   total porosity than flow along the layering, though still substantially less than the amount of total porosity. Whitby

373   shale (Mckernan et al., 2017) displays the same effect. In marked contrast, for the Pennant sandstone $\xi = 2.72$. This

374   is close to the value of $\xi = 2.67$ corresponding to the total porosity (4.6%) of the rock, implying a high degree of

375   connectivity between the pore spaces in Pennant sandstone.

376

377

Solid Earth
Discussions
Open Access
EGU
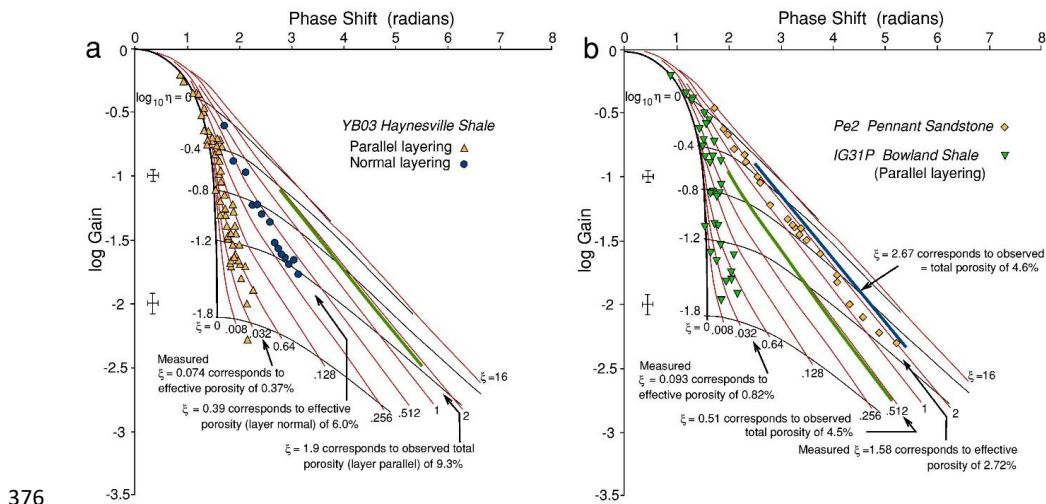
378   **Figure 5. Log gain vs phase angle data from oscillating pore pressure measurements on :**

379   **(a)** **Haynesville shale.** $\xi = 1.9$ **would correspond to total porosity 9.3% for flow in the sample parallel to**
380   **layering if all porosity participates in the flow. Observed** $\xi = 0.39$ **normal to layering is much greater**
381   **than parallel to layering** $\xi = 0.074$**, but both are substantially less than that corresponding to total**
382   **porosity. Flow parallel to layering only 'sees' or 'uses' about 4% of the total pore space, and normal to**
383   **layering about 42% of the total pore space.**
384   **(b)** **Bowland shale.** $\xi = 0.51$ **would correspond to total porosity 9.3% for flow in the sample parallel to**
385   **layering if all porosity participates in the flow. Observed** $\xi = 0.093$ **for flow parallel to the layering**
386   **corresponds to a conductive porosity (0.82%) much less than total porosity. In contrast, data for**
387   **Pennant sandstone show observed** $\xi = 1.58$ **to be closer to that** $\xi = 2.67$ **which corresponds to the**
388   **total porosity of the rock.**

389   **4.1.5 Bulk moduli of compressibility for Pennant sandstone**

390   Bulk modulus of porosity K_ϕ (defined in Eq. (2)) and its effective pressure sensitivity can be measured from the

391   volume of argon expelled from the rock during increments of confining pressure at constant pore pressure, and

392   K_{dry} can be calculated using Eq. (4) (Fig. 6a). K_o is the mineral bulk compressibility estimated as the VRH

393   average at zero porosity (given for these rocks in Table 1).

394   K_ϕ/ϕ is the value of the pore bulk modulus referred to the total volume of the rock, rather than to the pore space

395   volume. K_ϕ/ϕ and K_{dry} versus Terzaghi effective confining pressure are shown in Fig. 6 for Pennant Sandstone.

396   K_{dry} is asymptotic to K_o (41.5 GPa) at high pressure.

397   The pore pressure coefficient m, describing the effects of pore pressures on elastic distortions of a porous rock,

398   and defined in $P_{eff} = P_c(1 - m P_p)$ is given in terms of the bulk moduli K_{dry} and K_o in Eq. (7). In Fig. 7 the resultant

399   m versus effective pressure curves are shown for both Pennant sandstone and Haynesville shale. Bulk moduli are

400   isotropic properties with values unaffected even when the aggregate displays preferred orientation (shape and

401   crystallographic) of constituent grains (Andrews, 1978; Mendelson, 1981).

402

403   **Figure 6.**

Solid Earth
Discussions

Open Access

EGU
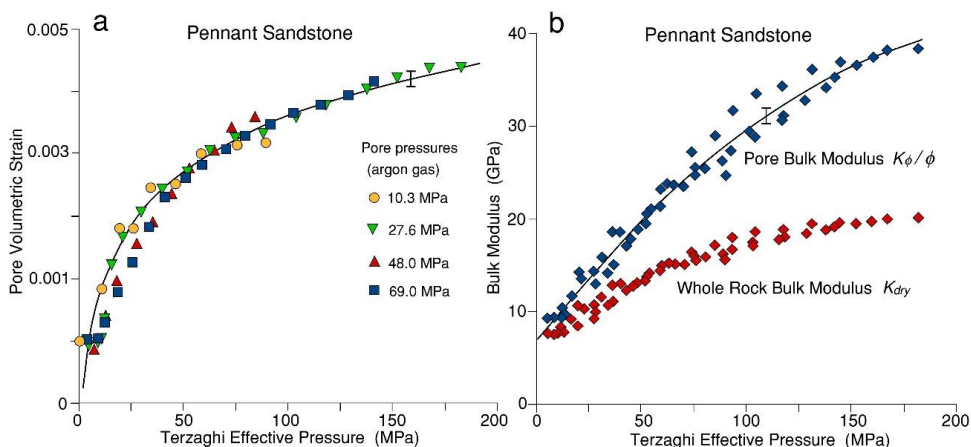
404   (a) **Volumetric strain (with respect to whole sample volume) for Pennant sandstone at four different**
405   **constant gas pore pressures. There is no significant effect of magnitude of pore pressure. About**
406   **20% of the total pore volume is elastically reduced over a range of 200 MPa effective pressure.**
407   (b) **Pore bulk modulus K_ϕ /ϕ from gas expulsion data in (a) for Pennant sandstone, and whole rock**
408   **bulk modulus calculated from K_ϕ /ϕ and K_o (41.5 GPa). Pore spaces become rapidly less compliant**
409   **as effective pressure increases.**
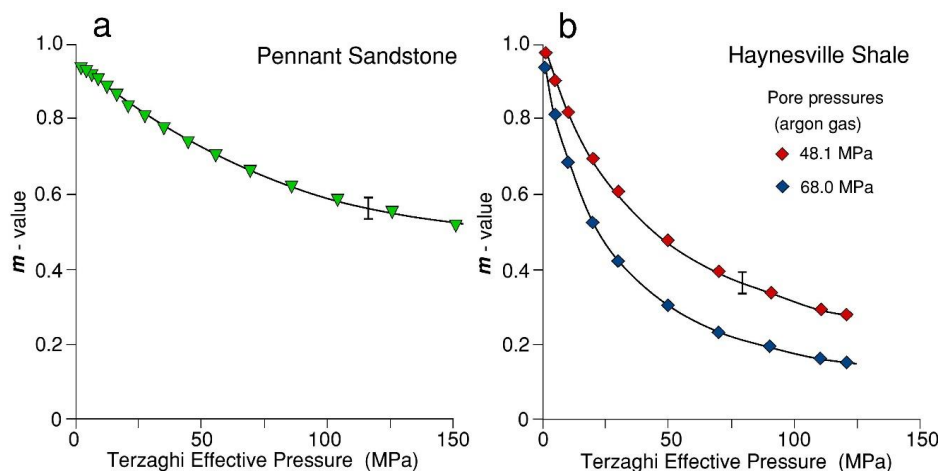

410

411   **Figure 7.**

412   ***m* from bulk modulus data and Eq. (7) for (a) Pennant sandstone and (b) Haynesville shale. The**
413   **decrease of *m* with P_{eff} arises from the stiffening of the pore spaces with effective pressure, and the**
414   **effect is greater for the shale than for the sandstone.**

415   At low pressure K_{dry} is much less than K_o, hence m approaches 1. As K_{dry} increases with pressure it approaches

416   K_o, hence m decreases with pressure, and will eventually reach zero when all pore space has collapsed. Any small

417   increase of K_o with pressure has been ignored (e.g. Calderón et al., 2007). The variation of m with pressure forms

418   the basis for describing the decrease in permeability observed as effective pressure increases.

419   **4.1.6 Bulk moduli of compressibility for Haynesville shale**

420   Pore volumometry by the expelled gas volume method during progressive increase in confining pressure was

421   carried out on the two shale samples used (Fig 8). The resolution of the pore volume change data is poor because

422   the specimen size was rather small (1.9 cm long). The rapid increase in slope translates to a rapid rise of calculated

423   K_{dry} compared to Pennant sandstone, until it is a substantial fraction of K_o (61 GPa). However, the total amount of

424   gas expelled corresponds to a closure of about 2% of the initial porosity (0.15% of the whole sample volume).

425   Figure 7b shows pore pressure coefficient m calculated from the pore volumometry. m decreases rapidly because

426   the K_{dry} value rises rapidly to become a substantial fraction of K_o. It is not clear why the measurements at two

427   different pore pressures are so different, but it is thought to be attributable to different degrees of gas trapping in

428   poorly connected pore spaces.
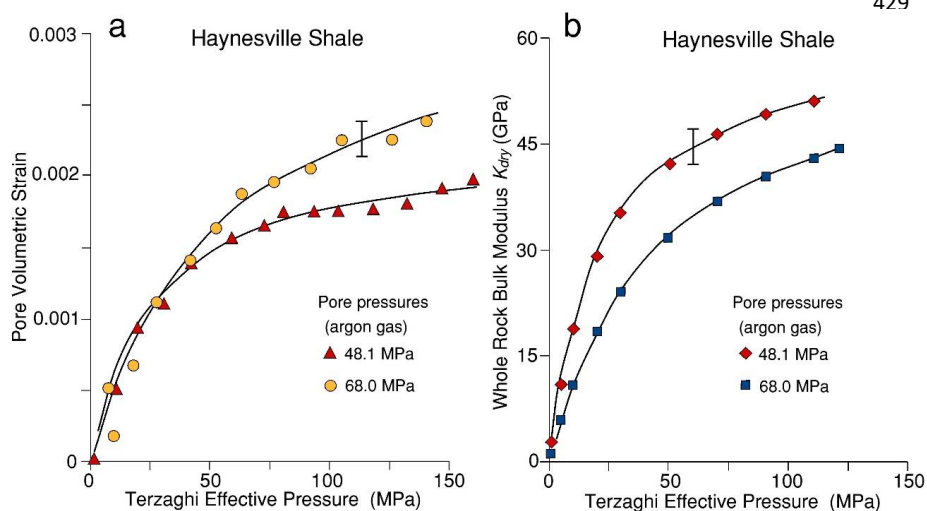
Figure 8.

(a) **Pore volumetric strain (as fraction of total specimen volume) vs Terzaghi effective pressure for Haynesville shale at the pore pressures indicated. Pore volume loss is approx. only 2% of the initial pore volume of the rock. Logarithmic fits to two of the data sets are shown.**
(b) **The gradients of the fitted lines in (a) correspond to the pore compressibility, and were used to obtain K_{dry} vs P_{eff}, as shown in (b) for the two pore pressures used. K_o= 61 GPa .**

4.1.7 Bulk moduli of compressibility for Bowland shale.
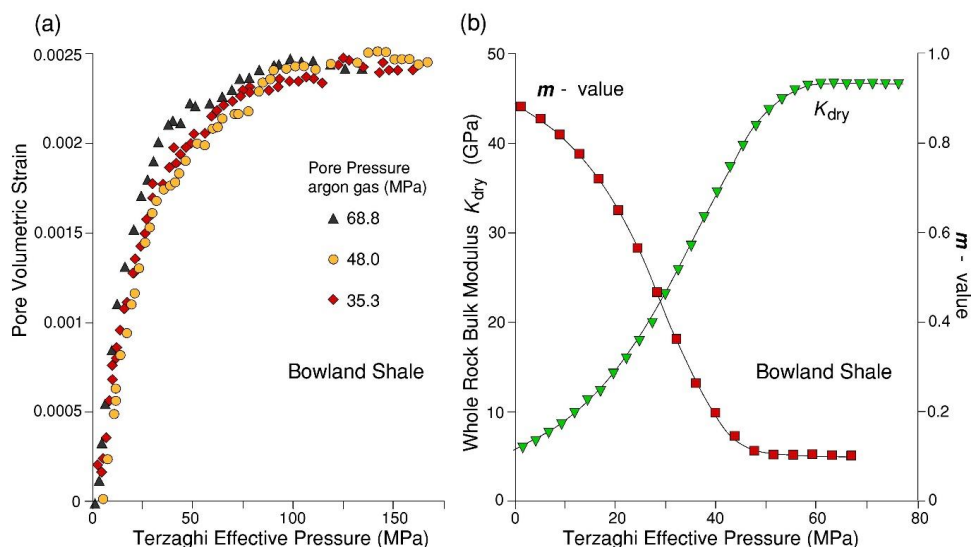
Figure 9.

(a) Pore volumometry of Bowland shale at 34.5, 48 and 69 MPa gas pore pressure. There is no significant difference at the three pore pressures, so that a single polynomial function can be fitted to all the data. The slope of the curves corresponds to the pore compressibility, which decreases markedly with increasing effective pressure.

452   **(b) Shows calculated K_{dry} bulk modulus of the sample (pore pressure = 69 MPa) from pore volumometry**
453   **measurements (inverted triangle symbols). K_o = 52.8 MPa. Also plotted is the m value from pore**
454   **volumometry (square symbols) for Bowland shale at 69 MPa pore pressure.**

455   A large specimen (25 mm diameter and 50 mm long) was used for these measurements on Bowland shale, cored

456   parallel to the layering. Because this is a low permeability rock, a 2 mm thick longitudinal slab of porous sintered

457   stainless steel was deployed as described earlier, to facilitate gas flow between the rock pores and the pore

458   pressure system. During pressure cycling it was necessary to correct data for the storativity of this plate. Figure 9

459   shows pore volumometry at 34.5, 48.1 and 69 MPa MPa argon gas pore pressure and K_{dry} data for Bowland shale.

460   Measurements were very reproducible and, unlike the Haynesville shale sample, there was no significant effect of

461   the magnitude of the pore pressure used. The amount of gas expelled during an effective confining pressure cycle

462   of 150 MPa corresponds to closure of ~8.4% of the initial (4.5% porosity) pore space, or about 0.04% of the total

463   rock volume. As also observed for Haynesville shale, this represents a very small fraction of the total porosity.

464   The poroelastic coefficient *m* calculated from the volumometry data is shown in Fig. 9b. Like the Haynesville

465   shale, the poroelastic coefficient obtained from pore volumometry decreases substantially with Terzaghi effective

466   pressure but does so at a similar rate to the Haynesville shale.

467

468   ## 5.   Discussion

469   ### 5.1 Generation of pore pressure during undrained loading

470   If drainage channelways become constricted during application of increments of P_c whilst P_p is also high, the

471   rock might become effectively undrained and hence pore pressure increments can arise. The magnitude of an

472   induced pore pressure under undrained conditions can be estimated from the Skempton parameter B, where

473
$$dP_p(\text{induced}) = BdP_c = \frac{C_{PP} + C_0}{C_{PP} + C_f}\, dP_c \qquad (10)$$

474   B is the Skempton B parameter of soil mechanics (Lockner and Stanchits, 2002). C_{pp} is the compressibility of the

475   pore space arising from a change in pore pressure, and is usually much less than the compressibility of the pore

476   fluid C_f. Thus B will lie between 0 and 1.0. Because usually $C_{pp} \gg C_o$ (where $C_o = 1/K_o$),

477
$$B \approx \frac{C_{PP}}{C_{PP} + C_f} = \frac{1}{1 + \dfrac{C_f}{C_{PP}}} \qquad (11)$$

478   For a gas saturated rock $C_f > C_{pp}$, hence $B \to 0$, and a gas-saturated rock will therefore never develop appreciable

479   pore pressures, especially at high porosities and from low initial gas pressures even when undrained, hence was

480   not considered to be an issue in the present experiments.

481   For a liquid-saturated rock however, this will not be true. B will approach 1 when $C_{pp} \gg C_f$. For liquid-

482   saturated porous sandstones under hydrostatic loading, Green and Wang (1986) found that under undrained

483   conditions, induced pore pressures were close to the applied confining pressures over a range of 60 MPa confining

484   pressure, thus the mean externally applied stress is almost totally transferred to the pore fluid via the

485   compressibility of the pore spaces.

486   The time constant for the dissipation of excess pore pressure in a region of characteristic dimension L in a

487   material of permeability k is on the order of

488    $$t = \frac{\phi \mu (C_{\text{f}} + C_{\text{PP}}) L^2}{k} \qquad (12)$$

489   t is the time required for pressure to decay by factor 1/e at distance L. The ratio $k / \mu (C_{\text{f}} + C_{\text{pp}})$ is the hydraulic

490   diffusivity κ (dimensions m²/s). For water, viscosity μ is 0.001 Pa s. Taking the bulk modulus K_{f} (= 1/fluid

491   compressibility, C_{f}) to be 2 GPa, and the permeability to be $10^{-18.5}$ m² for Haynesville shale at about 5 MPa

492   effective pressure (this is the highest permeability measured, which would apply after an excess fluid pressure had

493   been generated by compaction), $\kappa \sim 2 \times 10^{-6.5}$ m²/s. This leads to $t = 30$ sec for $L = 2$ cm. Time t is shorter by a

494   factor 1/30 when the pore fluid is gas owing to its lower viscosity (Gosman et al., 1969). This equation is for

495   constant k, but when k is a strong function of P_{eff}, decreasing perhaps 300-fold at high effective pressures, up to 5

496   minutes may be required for small pore pressure transients to decay.

497   **5.2 Simple model for pressure-dependence of permeability**

498   The simplest approach to describing the influence of pore space geometry and connectivity on permeability is to

499   regard the pores as a bundle of circular capillary tubes, so that the equation for viscous Poiseuille flow can be

500   applied and permeability calculated as a function of capillary tube radius. The circular capillary tube is a special

501   case of flow through tubes of elliptical cross section. In this case the flow rate then becomes acutely sensitive to

502   the short radial dimension of the tube, and the more eccentric the tube cross-section the greater will be the

503   sensitivity of its shape to externally applied effective pressure (Seeburger and Nur, 1984). Ma et al. (2018) imaged

504   connected pores spaces in shales, including Haynesville shale, as thin, crack-like shapes lying parallel to bedding

505   and of nanometric widths. Such pores in shales are not identical to straight capillary tubes of elliptical cross

506   section, but we can explore the extent to which the pressure sensitivity of observed permeability can be modelled

507   as such (Mckernan et al., 2017).

508   For a single tube of long axis $2c$ and short axis $2b$ the volume flow rate q of a fluid of viscosity μ along a

509   hydraulic pressure gradient dP_{p}/dx is well known to be

510    $$q = \frac{\pi}{4\mu} \left(\frac{b^3 c^3}{b^2 + c^2} \right) \left(\frac{\text{d}P_{\text{p}}}{\text{d}x} \right) \qquad (13)$$

511   and for N parallel tubes embedded in an elastic matrix of volume V and intersecting a 1 m² area normal to their

512   length the total flux $Q = Nq$. Separating out the viscosity and pressure gradient, the permeability k_o of the array is

513    $k_o = (N \pi / 4) (b^3 c^3/(b^2 + c^2))$.   Dimension c does not change with externally applied pressure for the elliptical

514   crack, whereas for the tapered crack it does, such as to keep the aspect ratio approximately constant (Mavko and

515   Nur, 1978), and Seeburger and Nur (1984) found that there is little difference in the effect of hydrostatic pressure

516   on flow rate when the tube cross section is elliptical or tapered. In terms of aspect ratio of an assumed elliptical

517   cross section $\alpha = b/c$, thus

518    $$k = \frac{N\pi}{4} c^4 \left(\frac{\alpha^3}{1 - \alpha} \right) \qquad (14)$$

18

519   The porosity $\phi = N\pi\, b\, c$. Parameters α, c and N that satisfy Eq. (4) are non-unique. N can be increased whilst pore

520   aperture is decreased, keeping k unchanged. A further constraint is therefore required, and this is provided by the

521   porosity ϕ, which is already known as a property of the material. Porosity is given by $\phi = N c^2 \alpha \pi$. Thus Eq. (14)

522   becomes

523
$$k = \frac{\phi c^2}{4}\left(\frac{\alpha^2}{1-\alpha^2}\right) \qquad (15)$$

524   Applying a hydrostatic pressure P to a solid bearing elliptical cracks reduces the b dimensions of all pore spaces,

525   and hence reduces the hydraulic transmissivity. The spatial density of the ellipses is assumed to be sufficiently

526   small that the elastic strain fields of each do not interact significantly. From Seeburger and Nur (1984), following

527   Walsh (1965) and Mavko and Nur (1978) the bulk modulus K_{dry} of a solid of volume V containing N tubular

528   cracks of elliptical cross section and semi-major axis c is given by

529
$$\frac{1}{K_{dry}} = \frac{1}{K_0} + \frac{1}{K_0}\left[2Nc^2d\,\frac{1-v^2}{1-2v}\right]$$

530   Thus

531
$$\frac{K_0}{K_{dry}} - 1 = 2Nc^2d\,\frac{1-v^2}{1-2v} \qquad (16)$$

532   d is the elliptical section tube length in the third dimension ($= V^{(1/3)}$).

533   Taking $m = (1 - K_{dry}/K_o)$, the left hand side is $m/(1-m)$, and the expression can be rearranged with c^2 on the

534   left side:

535
$$c^2 = \left(\frac{m}{1-m}\right)\left(\frac{1-2v}{1-v^2}\right)\frac{1}{2Nd} \qquad (17)$$

536   This can replace c^2 in Eq. (17), to give :

537
$$k = \left(\frac{\phi}{8Nd}\right)\left(\frac{\alpha^2}{1+\alpha^2}\right)\left(\frac{m}{1-m}\right)\left(\frac{1-2v}{1-v^2}\right) \qquad (18)$$

538   m is measured by pore volumometry as a function of Terzaghi effective pressure hence k is a function of effective

539   pressure. For $b \ll c$ it is primarily the reduction of the b dimension with increasing pressure that reduces

540   permeability. However, Mavko and Nur (1978) and Seeburger and Nur (1984) showed that the bulk modulus of a

541   porous solid of given porosity is not affected by the shape (eccentricity) of the pores. All pores change volume by

542   the same fractional amount. Only the distortion under pressure of the more eccentric ones is likely to affect the

543   permeability, although all pores will affect the storativity, according to how well connected they are. The

544   'connected' porosity estimated from the log gain versus phase shift plot, that is much smaller than the total

545   porosity, is used in Eq. (18). Its small value implies that most of the porosity is not being inflated during the

546   passage of the pore pressure wave, hence during the time-scale of the pressure oscillation the greater part of the

547   porosity is closed off by the action of the effective pressure.

548   Eq. (18) can be fitted to the permeability data log $k = f(P_{eff})$ measured for rock types studied using the non-linear

549   least-squares fitting routine Solver in MS Excel, to estimate the parameters N, v and α. Via the inferred effective

19

550   porosity the conductive pore width can also be estimated. The results of the fitting exercise provide the parameters

551   for a bundle of capillary tubes that *behaves in the same way* as the measured rocks. This is not to say that the

552   geometric arrangement of a simple capillary tube bundle corresponds to the pore space configurations in these

553   rocks, nor that a solution can be found for all rocks. The pressure sensitivity lies in the function that describes *m* as

554   a function of pressure, obtained from pore volumometry, and incorporating the effective pressure coefficient *n*.

555   Figure 10 shows the fit to the data for the Pennant sandstone; fit parameters are in Table 3.
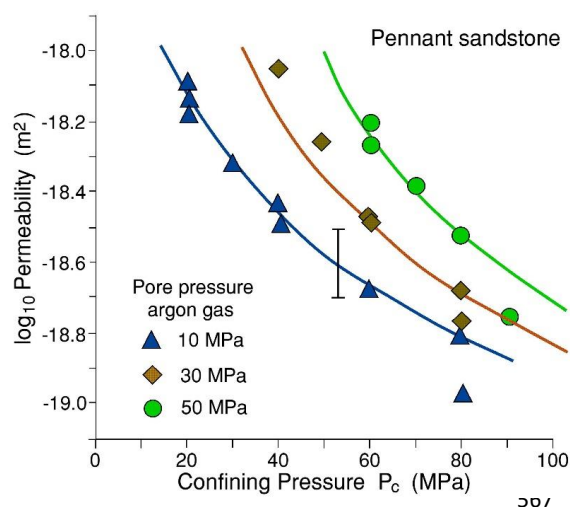
Figure 10. Gas permeability data for Pennant sandstone normal to layering, for three constant pore pressures. The three continuous curves are for Eq. (18) non-linear least-squares fits to the data.

Unlike the relatively homogeneous distribution of pore channels in the shales

568   down to the micron scale, in the Pennant sandstone the greater part of the rock volume is not porous, as it

569   comprises large quartz and feldspar grains. The 4.6% porosity is contained mostly in the spaces originally between

570   these grains that are now largely filled with phyllosilicate and oxide phases, i.e. about 26% of the total rock

571   volume, and is microstructurally in some ways comparable to a shale. Therefore in Table 3 the estimated

572   conductive channel dimensions are based on flow through this reduced volume fraction.

573   Figure 11 shows the fits to the permeability data for Haynesville shale. The cross-section shape of the elliptical

574   tubes is extremely eccentric and the shorter width of the tubes is measured in nanometres. This is consistent with

575   the observations of the dimensions of connected bedding-parallel porosity in the high-resolution tomography (CT)

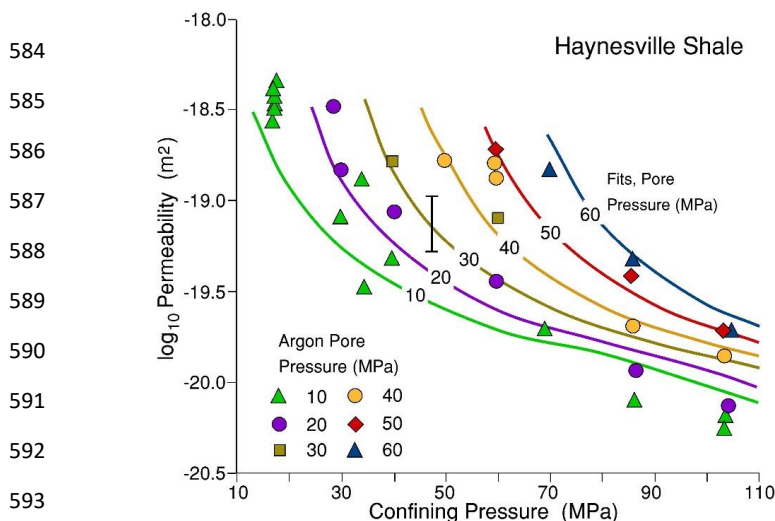576   observations of Ma et al. (2018) for Haynesville shale.

577

578

579

580

581

582

583

20

584
585
586
587
588
589
590
591
592
593

Figure 11. Permeability of Haynesville Shale versus total confining pressure for various values of constant gas pore pressure. The curves shown are the permeabilities calculated using the elliptical section pore channels model (Eq. (18)).

597

609
610
611
612
613
614
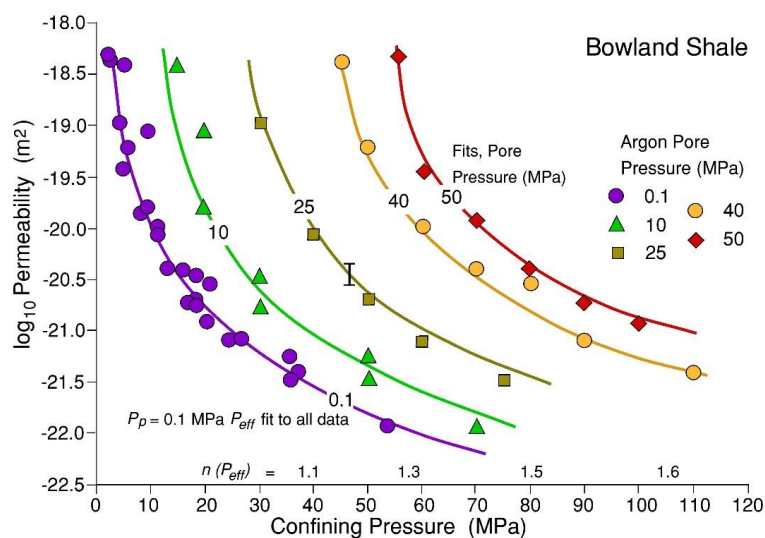
Figure 12. Permeability of Bowland Shale versus total confining pressure for various values of constant gas pore pressure. The curve and data shown for $Pp = 0.1$ is the effective pressure fit to all the data as shown in Fig. 3, collapsed onto a single least squares best-fit curve ($\log_{10}k = -0.503 \log_{10}P_{eff} -17.26$) for a pore pressure coefficient made to vary linearly with Terzaghi effective pressure according to $n = (1+P_{eff}(MPa)/85)$. Measured data for the separate pore pressures are shown, with best-fit curves with the variable pore pressure coefficient. n-values are shown to indicate how they increase from left to right.

Solid Earth

Discussions

Open Access

EGU
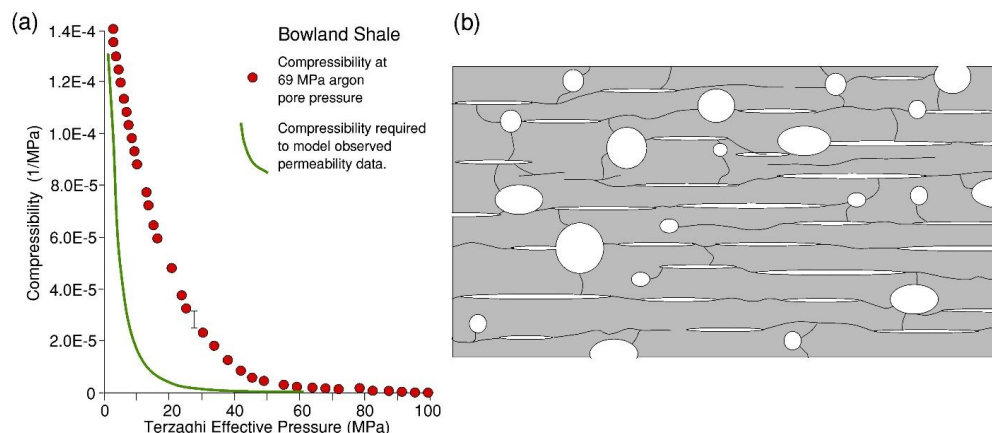
Figure 13.

(a) The experimentally observed variation of pore compressibility at 69 MPa pore pressure (filled circles) vs Terzaghi effective pressure for Bowland shale, derived from the data in Fig. 9. The reciprocal of this compressibility is ϕ/K_ϕ. This rate of reduction of compressibility with effective pressure cannot predict the observed pressure sensitivity of permeability that is observed experimentally. The continuous curve shows what the trend would have to be like in order that the single capillary tube model can behave in the same way as the rock.

(b) Schematic illustration of the porosity model best able to explain the permeability and bulk modulus data in the shales. Highly eccentric pores and cracks lie parallel to layering but are well-connected, accounting for easy gas transport yet using only a small fraction of the porosity. These narrow pores are easily constricted by hydrostatic pressure. Most of the storage capacity resides in the larger, equant pores of dimension about 1 micron that are poorly linked and not easily closed down by hydrostatic pressure.

Table 3. Fit parameters for the capillary tubes bundle model applied to describe the permeability of Haynesville shale and Pennant sandstone at low effective pressures, when the permeabilities are not strikingly different. n is the pore pressure multiplier for the permeability data, N is the number of pores intersecting a 1 m^2 area normal to the flow path, a is the pore shape aspect ratio and ν is the Poisson ratio. $2b$ is the mean short dimension (nm) of the elliptical cross section and s is the average pore spacing (microns).

644		Haynesville Shale	Pennant sst
645	n	0.99	0.86
646	N	1.03 E+11 m^{-2}	8.4 E+11 m^{-2}
647	α	0.0051	0.004
648	v	0.17	0.10
649	$2b$	13.5 nm	21 nm
650	s	3.1 μm	1.5 μm
651	Conductive porosity	0.3%	3.8%

652 --

653

654   The form of the curve of K_{dry} vs Terzaghi effective pressure does not permit the simple elliptical section

655   capillary tubes model to be fitted to Bowland shale, because the observed rate of decrease of m with effective

656   pressure is insufficiently rapid to explain the three orders of magnitude decrease of permeability observed over

657   this pressure range (see Fig. 12). Figure 13a compares the observed variation with effective pressure of pore

658   compressibility factor m to the variation that would be required to be able to make such a fit. It is inferred that

659   pressure must be able to act in this rock to close down pore connectivity in one or more additional ways to the

660   elastic compression of elliptical channel cross-sections. These could involve development of increased tortuosity

661   of channelways, or the existence of a more complex distribution of connected pores of different sizes and shapes.

662   The simple model of a set of similarly-sized and shaped channels that can behave in a comparable way to a real

663   pore network is clearly inapplicable to this rock.

664   **5.3 The effective pressure coefficients, m and n**

665   In the context of permeability, n is the multiplier of pore pressure in the definition of the modification of

666   Terzaghi effective pressure that brings observed permeability data at different constant pore pressures onto a

667   common curve (e.g. Fig. 12), thus $P_{eff} = P_c - nP_p$. n takes a value close to unity in the case of the experimental

668   data on Haynesville shale and Whitby shale, and 0.86 in the case of Pennant sandstone. In other studies, observed

669   departures from unity have been attributed to, for example, differences in the roles of elastically stiff and

670   elastically soft mineral components surrounding the pore spaces in responses to changes in P_c relative to changes

671   in P_p (e.g. Zoback and Byerlee, 1975; Kwon et al., 2001; Ma and Zoback, 2017), resulting in different rates of

672   change of pore volume with P_c and P_p.

673   On the other hand, in Eq. (4), for a homogeneous, isotropic elastic matrix, it is the value of K_{dry}, the bulk

674   modulus of the porous rock, that determines the change in geometry of pore spaces, and hence permeability, in

675   response to effective pressure change. The theoretical expression for the effective pressure coefficient m for elastic

676   *deformations* of a mechanically linear, homogeneous and isotropic rock is given by Eq. (7) and this parameter

677   appears in the expression for the permeability according to the bundle of capillary tubes model (Eq. (18)). Using

678   the pore fluid displacement method (Figs. 6, 8 and 9) we have found that in all cases m decreases from near unity

679   with Terzaghi effective pressure according to the pressure dependence of K_{dry}, whereas for Pennant sandstone and

680   Haynesville shale, observed *n* remains close to unity for permeability data and exceeds unity for Bowland shale

681   over Terzaghi effective pressures from zero to *ca* 80 MPa, thus $m \neq n$. Nur and Byerlee (1971) took care to point

682   out that *m* as defined in Eq. (7) cannot generally be used as a predictor of effective pressure coefficient for

683   particular processes, like permeability, mechanical strength and elastic wave velocities, even though all involve

684   elastic distortions.

685   As was pointed out earlier, pressure sensitivity of permeability according to the simple capillary bundle model

686   cannot behave in the same way as was observed experimentally for Bowland shale. Also, a single value of *n*

687   cannot reconcile permeabilities at different pore pressures for this rock. Figure 12 shows the permeability data for

688   Bowland shale separated into measurements at different pore pressures. By extending the collective fit between

689   log permeability and effective pressure shown in Fig. 12 to the data at each pore pressure, the downward

690   divergence of the curves becomes apparent. This can be described empirically by fitting a linear variation of *n*

691   with Terzaghi effective pressure, such that $n = 1$ at low effective pressures, rising to $n = 1.6$ at the upper end of the

692   pressure range used. This is interpreted as a further manifestation of the pore structure complexities that mean that

693   this Bowland shale cannot be described by a simple capillary tube bundle model.

694   **5.4 Relationship between observed pressure-dependent permeability and mineralogy**

695   Several studies have reported the relationships between mineralogy of shales and related rocks and their

696   petrophysical properties (e.g. Kwon et al., 2004; Ma and Zoback, 2017). The rocks used in this study display a

697   spectrum of mineralogy that is reflected in their permeabilities, both in terms of absolute values and their

698   sensitivity to effective pressure.

699   Pennant sandstone is typical of tight gas sands in which the load bearing framework is of continuous quartz and

700   feldspar grains with what would otherwise be a large porosity that is mostly filled with some detrital muscovite

701   plus diagenetically-introduced clay and oxide phases (Wilson and Pittman, 1977; Howard, 1992). Prior to the pore

702   filling there was a degree of intergranular pressure solution and formation of quartz overgrowths around quartz

703   grains. The protective armour around the filled pore spaces afforded by the quartz framework is thought to have

704   limited degree of compaction of the pore filling, in which most of the present porosity resides. Relative to the

705   volume of the inter-quartz spaces, the porosity of the filling would be ~20%, and it is thought that this contributes

706   to the relatively high overall permeability and reduced pressure sensitivity of Pennant sandstone.

707   The Bowland and Haynesville shales are mineralogically and microstructurally strikingly different. It is

708   important to remember that these are particular samples taken from their respective sequences and may not be

709   especially representative of their host sequences at all. The Bowland shale sample is a phyllosilicate-rich,

710   carbonate-poor siliceous mudstone with sufficient phyllosilicate to form a contiguous matrix, and this is likely to

711   be responsible for the relatively low bulk modulus (53 GPa) of the rock and hence low permeability. The

712   Haynesville shale is a carbonate-rich (>50vol%), phyllosilicate-poor siliceous mudstone with a higher bulk

713   modulus (61 GPa). The carbonate grains (fossil fragments and diagenetic carbonate) provide a stiff framework of

714   contiguous grains, helping to maintain open porosity and to resist its elastic compaction. Despite these qualitative

715   observations that can be made about how mineralogy and microstructure impacts upon permeability, the present

716   results do not form a basis for making any quantitative correlations.

717

718 **5.5 Inference of key characteristics of pore space geometry in shales**

719   Much has been written on pore space geometry based on SEM, TEM and Xray CT imaging of shales, but
720 important characteristics can be inferred from observations of bulk petrophysical properties. Key points noted in
721 the present study are:

722 ● The storativities for both shales are extremely small for flow paths lying parallel to the layering, such that over
723 90% of the available pore space is not participating in the flow.

724 ● At low effective pressures, the permeabilities of all three rocks are similar, but with increasing effective
725 pressures they diverge at markedly different rates. Marked sensitivity of permeability to effective confining
726 pressure implies that conductive (well-connected) pores are flat and crack-like. This is supported by permeability
727 modelling, that suggests that for a bundle of elliptical-section capillary tubes of equivalent permeability behaviour,
728 their aspect ratios are extremely small and the narrow dimension is expected to be in the nanometric range (Table
729 3).

730 ● For flow normal to layering, at least in Haynesville shale, storativity is much greater than for flow across the
731 layering, but still implies that over half of the pore space is not participating in the flow.

732 ● Permeability in both shales is very low under elevated effective pressures compared to Pennant sandstone,
733 which is of similar overall porosity, implying that connected pore spaces are narrow and/or poorly
734 connected/tortuous.

735   The above observations suggest that the effective configuration of pores spaces corresponds to the sketch shown
736 in Fig. 13b, with a population of highly oriented, crack-like pores parallel to layering that account for only a small
737 fraction of the total porosity but dominate the hydraulic transmissivity through the rock mass parallel to the
738 layering and also account for the low storativity associated with flow along the layering. These are poorly
739 connected to larger, probably more equant pores by conduction channels trending across the layering, and which
740 contain most of the gas storage space in the rock. The equant pores are 'seen' more easily for flow across the
741 layering, so that this flow is characterised by higher storativity, as demonstrated for Haynesville shale. Such
742 storage pores are likely to be much slower to drain (or to fill) in response to an applied pore pressure gradient than
743 implicit in the laboratory-measured permeability data. This suggests that permeabilities measured by transient
744 flow methods in the laboratory may lead to an over-conservative estimate of the potential for drainage of a gas
745 reservoir in shale, and perhaps help partially to explain the long-term persistence of flows from some shale gas
746 reservoirs (e.g. Guo et al., 2017; Wang, 2017).

747   **6. Conclusions**

748   Permeabilities as functions of effective pressure were measured using the oscillating pore pressure method at 20
749 ºC for three rocks (Haynesville and Bowland shales and Pennant sandstone) of low permeabilities and comparable
750 porosities. Tests were at effective pressures ranging up to 90 MPa with argon gas as permeant. From exhibiting
751 comparable permeabilities at low pressures they diverged markedly with increasing pressure. Pennant sandstone
752 showed permeability reduction with pressure of less than ten-fold, Haynesville shale became less permeable by
753 almost two orders of magnitude, whereas Bowland shale was reduced in permeability by more than 3 orders of
754 magnitude. The different pressure sensitivities of permeability correlated inversely with their (pressure sensitive)

755   bulk moduli and qualitatively with mineralogical differences, going from a continuous framework of stiff quartz

756   grains (sandstone) through a carbonate-rich framework (Haynesville shale) to a contiguous matrix of phyllosilicate

757   grains (Bowland shale).

758   High storativity of the sandstone implied that most of the available pore space was involved in the gas flow, but

759   in the shales, for flow parallel to the layering, less than 10% of the available pore space was involved in the flow.

760   For flow in the Haynesville shale across the layering a larger pore space fraction was involved, but still much less

761   than all the available pore space. Thus only a small fraction of the total pore space can be inferred to be well

762   connected in the shales. This implies that whilst the permeability we measure in the oscillating pore pressure

763   experiment is that associated with gas transport through the rock mass, a lower effective permeability applies to

764   the ability of the gas to flow into and out of the storage pores.

765   A simple model of permeability was developed based upon connected pore space behaving in a way similar to a

766   bundle of capillary tubes of highly eccentric cross section. By fitting the model to the experimental data, it was

767   possible to demonstrate that this model behaved in a similar way to the rocks for the case of Pennant sandstone

768   and Haynesville shale, but the model could not behave in a way compatible with the marked pressure sensitivity of

769   permeability for the Bowland shale. It was inferred that a more complex distribution of connected pore spaces of

770   varying dimension and tortuosity would be required to behave like the Bowland shale sample.

771   **Author contribution**

772   EHR was responsible for the conceptualization and methodology of the study, carrying out the bulk of the

773   experiments, compilation and analysis of data and writing the manuscript. JM was responsible for the acquisition

774   and management of financial support, carrying out the FEM analysis, contribution to experimental design and data

775   presentation, and preparation of the paper. YB carried out the experiments on Haynesville shale under the

776   supervision of JM and EHR as part of his doctoral research.

777   **Data availability**

778   All of the experimental data acquired in this research is freely accessible and collated in supporting datafile

779   DF1.csv. In correspondence with UK Research Council requirements is deposited in the UK National Geoscience

780   Data Centre, identified by the title of this paper. It is also downloadable from https://zenodo.org/record/5675601
     The Authors declare that they have no conflict of interests.

789   thick SIKA R1AX porous stainless-steel plates used in this work. Experimental Officers Stephen May and Lee

790   Paul contributed to equipment maintenance. Mike Chandler and Rochelle Taylor provided helpful discussions.

791   **References**

792   Andrews, K. W.: Elastic moduli of polycrystalline cubic metals. Journal of Physics D: Applied Physics, 11, 2527-
793   2534, 1978.
794
795   Bernabé, Y., Mok, U. and Evans, B.: A note on the oscillating flow method for measuring rock permeability.
796   International Journal of Rock Mechanics and Mining Sciences, 43(2), 311–316.
797   https://doi.org/10.1016/j.ijrmms.2005.04.013, 2006.

798   Biot, M. A. and Willis, D. G.: The Elastic Coefficients of the Theory of Consolidation. Journal of Applied
799   Mechanics, 24, 594-601, 1957.
800
801   Brace, W. F., Walsh, J. B. and Frangos, W. T.: Permeability of granite under high pressure. Journal of
802   Geophysical Research, 73(6), 2225–2236. https://doi.org/10.1029/JB073i006p02225, 1968.

803   Bustin, R. M., Bustin, A.M.M., Cui, A., Ross, D., Pathi, V.M. and others.: Impact of shale properties on pore
804   structure and storage characteristics. Paper presented at the SPE Shale Gas Production Conference, 16–18
805   November 2008, Fort Worth, Texas, USA, 2008.
806
807   Calderón, E., Gauthier, M., Decremps, F., Hamel, G., Syfosse, G. and Polian, A.: Complete determination of the
808   elastic moduli of α-quartz under hydrostatic pressure up to 1 GPa: an ultrasonic study. J. Phys.: Condens. Matter,
809   19, 436228, doi:10.1088/0953-8984/19/43/436228, 2007.

810   Cui, X., Bustin, A. M. M. and Bustin, R. M.: Measurements of gas permeability and diffusivity of tight reservoir
811   rocks: different approaches and their applications. Geofluids, 9(3), 208–223. https://doi.org/10.1111/j.1468-
812   8123.2009.00244.x, 2009.

813   Diaz, H. G., Fuentes, C. C., Calvin, C., Yang, Y., MacPhail, K. and Lewis, R.: Evaluating the impact of
814   mineralogy on reservoir quality and completion quality of organic shale plays. In: AAPG Rocky Mountain Section
815   Meeting, Salt Lake City, Utah, pp. 22–24, 2013.
816
817   Dowey, P. J. and Taylor, K. G.: Diagenetic mineral development within the Upper Jurassic Haynesville-Bossier
818   Shale, USA. Sedimentology 67, 47–77, doi: 10.1111/sed.12624, 2020.
819
820   Faulkner, D. R., and Rutter, E. H.: Comparisons of water and argon permeability in natural clay-bearing fault
821   gouge under high pressure at 20°C. Journal of Geophysical Research: Solid Earth, 105(B7), 16415–16426.
822   https://doi.org/10.1029/2000jb900134, 2000.

823   Fischer, G . J., and Paterson, M. S.: Measurement of permeability and storage capacity in rocks during
824   deformation at high temperature and pressure. In Fault Mechanics and Transport Properties of Rocks, edited by B.
825   Evans and T.-f. Wong, 213-251, Academic Press, San Diego, Calif., 1992.
826
827   Gosman, A. L., McCarty, R. D. and Hust, J. G.: Thermodynamic properties of argon from the triple point to 300 K
828   at pressures to 1000 atmospheres. In: National Standard Reference Data Series, National Bureau of Standards, 27.
829   Washington, DC: US Department of Commerce, 1969.
830
831   Green, D. H. and Wang, H. F.: Fluid pressure response to undrained compression
832   in saturated sedimentary rock. Geophysics 51, 948–956, 1986.

833   Guo, K., Zhang, B., Wachtmeister, H., Aleklettb, K. and Höök, M.: Characteristic Production Decline Patterns for
834   Shale Gas Wells in Barnett. International Journal of Sustainable Future for Human Security, J-Sustain. 5, 12-21.
835   DOI: 10.24910/jsustain/5.1/1221, 2017.

836   Hammes, U., Hamlin, H. S. and Ewing, T. E.: Geologic analysis of the Upper Jurassic Haynesville Shale in east
837   Texas and west Louisiana. AAPG Bull. 95, 1643–1666, 2011.
838
839   Hackston, A. and Rutter E.H.: The Mohr–Coulomb criterion for intact rock strength and

840   friction—a re-evaluation and consideration of failure under polyaxial stresses. Solid Earth **7**,
841   493–508. (doi:10.5194/se-7-493-2016), 2016.
842
843   Hasanov, A. K., Dugan, B. and Batzle, M. L.: Numerical simulation of oscillating pore pressure experiments and
844   inversion for permeability. Water Resources Research, 56, e2019WR025681.
845   https://doi.org/10.1029/2019WR025681, 2020.
846
847   Hasanov, A. K., Dugan, B., Batzle, M. L. and Prasad, M.: Hydraulic and poroelastic rock properties from
848   oscillating pore pressure experiments. Journal of Geophysical Research: Solid Earth 124, 4473–4491.
849   https://doi.org/10.1029/ 2018JB017276, 2019.
850
851   Heller, R., Vermylen, J. and Zoback, M.: Experimental investigation of matrix permeability of gas shales.
852   American Association of Petroleum Geologists Bulletin, 98, 975–995, 2014.
853
854   Howard, J. J.: Influence of authigenic clay minerals on permeability. In: (David W. Houseknecht and Edward D.
855   Pittman; Eds), Origin, Diagenesis, and Petrophysics of Clay Minerals in Sandstones. SEPM Special Publication
856   47, 257-264. DOI:10.2110/pec.92.47.0257, 1992.

857   Kelling G.: Upper Carboniferous sedimentation in South Wales. In *The Upper Palaeozoic and post-Palaeozoic*
858   *rocks of Wales* (ed. T.R. Owen), pp. 185–224. Cardiff, UK: University of Wales Press, 1974.
859
860   Kranz, R. L., Saltzman, J. S. and Blacic, J. D.: Hydraulic diffusivity measurements on laboratory rock samples
861   using an oscillating pore pressure method. International Journal of Rock Mechanics and Mining Sciences 27(5),
862   345–352. https://doi.org/10.1016/0148-9062(90)92709-N, 1990.

863   Kwon, O., Kronenberg, A. K., Gangi, A. F. and Johnson, B.: Permeability of Wilcox shale and its effective
864   pressure law. J. Geophys. Res. 106, 19,339–19,353, doi:10.1029/2001JB000273, 2001.
865
866   Kwon, O., Kronenberg, A. K., Gangi, A. F., Johnson, B. and Herbert, B. E.: Permeability of illite-bearing shale: 1.
867   Anisotropy and effects of clay content and loading, J. Geophys. Res. 109, B10205, doi:10.1029/2004JB003052,
868   2004.
869
870   Lazar, O. R., Bohacs, K. M., Macquaker, J. H. S., Schieber, J. and Demko, T. M.: Capturing key attributes of
871   finegrained sedimentary rocks in outcrops, cores, and thin sections: nomenclature and description guidelines. J.
872   Sed. Res. 85, 230–246, 2015.
873
874   Lockner, D. A. and Stanchits, S. A.: Undrained Poroelastic Response of Sandstones to Deviatoric Stress Change.
875   J. Geophys. Res. 107, 2353, doi:10.1029/2001JB001460, 2002.
876
877   Ma, L., Slater, T., Dowey, P. J., Yue, S., Rutter E. H., Taylor, K. G. and Lee, P. D.: Hierarchical integration of
878   porosity in shales. Scientific Reports, 8:11683, DOI:10.1038/s41598-018-30153-x, 2018.
879
880   Ma, X. and Zoback, M. D.: Laboratory experiments simulating poroelastic stress changes associated with
881   depletion and injection in low porosity sedimentary rocks, J. Geophys. Res. Solid Earth 122, 2478–2503,
882   doi:10.1002/2016JB013668, 2017.
883
884   Mavko, G. M. and Nur, A.: 1978. The effect of nonelliptical cracks on the compressibility of rocks. Journal of
885   geophysical research, 83, 4459-4468.
886
887   Mavko, G., Mukerji, T. and Dvorkin, J., The rock physics handbook: tools for seismic analysis of porous media,
888   Cambridge, Cambridge University Press. Cambridge, UK. (Vol. 112, Issue 483).
889   https://doi.org/10.1192/bjp.112.483.211-a, 2009.

890   McKernan, R., Mecklenburgh, J, Rutter, E. H. and Taylor, K. G.: Microstructural controls on the pressure-
891   dependent permeability of Whitby mudstone. In: Rutter, E. H., Mecklenburgh, J. and Taylor, K. G. (eds)
892   Geomechanical and Petrophysical Properties of Mudrocks. Geological Society, London, Special Publications, 454,
893   39-66. doi.org/10.1144/SP454.15, 2017.
894
895   Mendelson, K. S.: Bulk modulus of a polycrystal, J. Phys. D: Appl. Phys.14 1307-1309, 1981.
896

897 Michels, S., Botzen, A., and Schuurman, W.: The viscosity of argon at pressures up to 2000 atmospheres. Physica
898 20(7-12), 1141–1148. https://doi.org/10.1016/S0031-8914(54)80257-6, 1954.
899

900 Mondol, N. H., Jahren, J. and Bjørlykke, K.: Elastic properties of clay minerals. The Leading Edge, 27, 758-770,
901 2008.
902

903 Nur, A. and Byerlee, J. D.: An exact effective stress law for elastic deformation
904 of rocks with fluids. Journal of Geophysical Research, 76, 6414–6419, 1971.
905

906 Rutter E. H. and Hackston, A.: On the effective stress law for rock-on-rock frictional sliding, and fault slip
907 triggered by means of fluid injection. *Phil. Trans. R. Soc. A* 375: 20160001.
908 http://dx.doi.org/10.1098/rsta.2016.0001, 2017.
909

910 Rutter E. H., and Mecklenburgh J.: Hydraulic conductivity of bedding-parallel cracks in shale as a function of
911 shear and normal stress. In: Geomechanical and petrophysical properties of mudrocks, Geological Society of
912 London Special Publication vol. 454 (eds E. Rutter, J. Mecklenburgh, K. Taylor). London, UK: Geological
913 Society of London. doi:10.1144/SP454.9, 2017.
914

915 Rutter, E. H. and Mecklenburgh, J.: Influence of Normal and Shear Stress on the Hydraulic Transmissivity of Thin
916 Cracks in a Tight Quartz Sandstone, a Granite, and a Shale: Journal of Geophysical Research: Solid Earth 123,
917 1262-1285, 2018.

918 Seeburger, D. A. and Nur, A.: A pore space model for rock permeability and bulk modulus. Journal of
919 Geophysical Research. 89, 527-536. https://doi.org/10.1029/JB089iB01p00527, 1984.

920 Skempton, A. W.: The pore pressure coefficient in saturated soils. Géotechnique 10, 186-187, 1960.

921 Terzaghi, K. V.: Die Berechnung der Durchassigkeitsziffer des Tones aus dem Verlauf der hydrodynamischen
922 Spannungserscheinungen, Sitzungsber. Akad. Wiss. Wien Math Naturwiss. Kl. Abt. 2A, 132, 125-138, 1923.
923

924 Walsh, J.: The effect of cracks on the compressibility of rock. Journal of Geophysical Research 70, 381–389.
925 https://doi.org/10.1029/jz070i002p00381, 1965.
926

927 Wang, H.: What Factors Control Shale Gas Production and Production Decline Trend in Fractured Systems: A
928 Comprehensive Analysis and Investigation. SPE Journal 22: 562-581. http://dx.doi.org/10.2118/179967-PA, 2017.

929 Wilson, M. D. and Pittman, E. D.: Authigenic clays in sandstones; recognition and influence on reservoir
930 properties and paleoenvironmental analysis . Journal of Sedimentary Research 47: 3–31.
931 doi.org/10.1306/212F70E5-2B24-11D7-8648000102C1865D, 1977.

932 Zee Ma, Y., Moore, W. R., Gomez, E., Clark, W. J. and Zhang, Y.: Tight Gas Sandstone Reservoirs, Part 1:
933 Overview and Lithofacies. Unconventional Oil and Gas Resources Handbook; Evaluation and Development,
934 Chapter 14. Elsevier, Amsterdam. 405-427 doi.org/10.1016/B978-0-12-802238-2.00014-6, 2016.
935

936 Zimmerman, R.W.: Compressibility of sandstones: Elsevier, Amsterdam, The Netherlands, 173 pp., 1991.

937 Zoback, M. D. and Byerlee, J. D.: Permeability and effective stress: Bull. Am. Assoc. Petr. Geol. 59, 154–158,
938 1975.
939